A Cavity Based X-ray FEL Demonstrator at the European XFEL facility*

Patrick Rauer,† Winfried Decking, Dirk Lipka, Daniel Thoden, and Torsten Wohlenberg
Deutsches Elektronen-Synchrotron DESY, Germany

Immo Bahns, Ulf Brueggmann, Sara Casalbuoni, Massimiliano Di Felice, Martin Dommach, Jan Grünert, Suren Karabekyan, Andreas Koch, Daniele La Civita, Benoit Rio, Liubov Samoylova, Harald Sinn, Maurizio Vannoni, and Christopher Youngman
European XFEL GmbH, Germany

Wolfgang Hillert and Joerg Rossbach
Universität Hamburg, Germany
(Dated: October 7, 2022)

In this article the concept of a recently funded R&D project for installation of a proof-of-concept cavity based X-ray free electron laser (CBXFEL) demonstrator experiment at the European XFEL facility is presented. It is composed of a X-ray cavity design in backscattering geometry with 133 m round trip length using cryogenically cooled diamond crystals. It employs the concept of retroreflection to reduce the sensitivity to vibrations. The FEL radiation is produced in four undulator segments of 20 m total length. Simulations at 16 GeV beam energy and 250 pC bunch charge show that the expected X-ray pulses in saturation surpass state of the art X-ray sources considering spectral flux and three-dimensional coherence. However, the stability of the proof of concept setup is severely challenged by the finite thermal transport in the diamond crystals. Therefore, suitable measures such as cooling the crystals to 70K are explained in this paper and additional ones will have to be developed in the course of this project.

I. INTRODUCTION

Current hard XFEL machines such as the *Linac Coherent Light Source* (LCLS), the *European XFEL* (EuXFEL), the *Spring-8 Angstrom Compact free-electron LAser* (SACLA), the SwissFEL and the *Pohang Accelerator Laboratory X-ray Free Electron Laser* (PAL-XFEL) are mainly using the self-amplified spontaneous emission (SASE) scheme for operation. While these sources produce very brilliant femtosecond X-ray pulses with excellent transverse coherence, they suffer from two major disadvantages. For one, they need very long undulator sections to reach saturation due to the initial seed being created by weak spontaneous emission. More fundamental is its rather low degree of monochromaticity on the order of 1 ‰ and the lack of longitudinal coherence as one radiation pulse consists of 100 to 10000s of longitudinal modes [1]. This is unlike classical optical lasers which can provide almost perfect longitudinal coherence, single mode, and outstanding monochromaticity better than 1×10^{-10}. In order to reach a lower frequency bandwidth on the order of 10^{-5} to 10^{-6} one needs to use crystal monochromators. These are selecting only a small portion of the SASE spectrum which is different from shot to shot, cutting away the majority of incident flux with the resulting transmitted radiation fluctuating by almost 100 %. Over the recent years, multiple schemes have been proposed and partly realized to improve this. *hard X-ray self seeding* (HXRSS) has already been successfully implemented [2–5] and has proven a powerful technique for improving the longitudinal coherence of hard X-ray FELs. Promising schemes still to be realized are the *X-ray Regenerative Amplifier FEL* (XRAFEL) proposed by *Z. Huang* in 2006 [6] and the *X-ray Free Electron Laser Oscillator* (XFELO) proposed by *K.J. Kim* in 2008 [7]. Latter two schemes are based on trapping FEL radiation inside a X-ray optical cavity, using monochromatizing crystals based on Bragg reflection instead of total reflecting optical mirrors [6, 8]. While the XFELO is closely related to the low gain FELO scheme, the XRAFEL is based on the strong gain FEL amplifier scheme. Both schemes can be summarized under the more general term *Cavity Based X-ray FEL* (CBXFEL), which will also be used throughout this publication. Due to the promise of delivering outstanding radiation properties, CBXFELs have received growing interest in the recent years [8–19]. European XFEL is developing an CBXFEL demonstrator to be integrated into the hard X-ray undulator system and beam line SASE1. The principle goal of the demonstrator is to prove the working concept - meaning seeding and increasing longitudinal coherence by several orders of magnitude over subsequent round trips, from synchrotron radiation to almost monochromatic FEL amplifier radiation. While not being optimized for user operation at the moment, the very high spectral densities of the output might prove interesting for selected user experiments in the future.

The scope of this paper is to outline the fundamentals of the CBXFEL-demonstrator project. In Section II basic considerations of the experimental setup will be described. In Section III results from simulations on the performance of the radiation produced by the CBXFEL-

* …
† patrick.rauer@desy.de

demonstrator will be presented. For more details on the CBXFEL-process at the EuXFEL, see ref. [20].

II. A CBXFEL-DEMONSTRATOR SETUP

The design of the CBXFEL-Demonstrator is kept as simple as possible. Features like wavelength tunability [8, 9] or involved out-coupling schemes are omitted. As sketched in Fig. 1 (top), the cavity is designed in a simple two crystal backscattering geometry. In between the crystals, four 5 m long variable gap undulator sections are positioned and chicanes are used to in- and out-couple the electrons. The chicanes prevent damage to the crystals while ensuring an electron beam well matched to the non-disturbed electron lattice. The crystal-to-crystal distance is fixed to $L_{C-C} \approx 66.42\,\mathrm{m}$, which matches an electron bunch repetition rate of $f_{\mathrm{rep}}^{\mathrm{el.}} = 2.25\,\mathrm{MHz}$. This is a repetition rate commonly used at the European XFEL accelerator, which agrees well with the spatial constraints in the tunnel and poses a good compromise between optical tolerances and heat load on the crystals. Due to multiple beam excitation and consequently degradation of the reflection efficiency at exact normal incidence in cubic crystals [21], the crystals are detuned by some milliradian by additional total reflecting mirrors. Furthermore, as optical stability of the cavity is essential [9] - especially keeping in mind the necessary transverse overlap of photon pulse and electron bunch - the cavity is decoupled to a large extent from both outer vibrations and pointing fluctuation of the incoming beam by arranging the crystals and two total reflecting mirrors orthogonal to each other. This forms a so called retroreflector as sketched in Fig. 1. Such a design will lead to a decrease in optical sensitivity to angular change of the mirror assembly by roughly two orders of magnitude. This increases the angular tolerance from roughly 100 nrad to at least $\approx 10\,\mu\mathrm{rad}$, which is much easier to achieve. One has to note, that this is only referring to the angular tolerance of the whole retroreflector assembly and not to the tolerance of the three individual elements in the assembly with respect to each other. For more details, the reader is referred to the appendix **B** or to [20].
Additionally, by applying a slight meridional curvature $R_m \approx 20\,\mathrm{km}$ along the long axis of the total reflecting mirrors, focusing of the X-ray pulses and therefore stabilization of the cavity can be achieved. An additional point quite uncommon for laser oscillators in general and X-ray oscillator in particular is the usage of two thick crystals ($t_C \approx 100\,\mu\mathrm{m}$) [22], being opaque for photons at the central reflection photon energy $E_c = 6.95\,\mathrm{keV}$ for C400 diamond in the angular darwin width of $\Delta\Theta_{\mathrm{DW}} \approx 5\,\mathrm{mrad}$ around the incidence angle of $\Theta_{in} = 4.38$, instead of one thick and one thin transmitting crystal. Such a setup, which was already proposed by *Huang and Ruth* in 2006 [6], will still transmit a considerable fraction of photon flux as will be explained in the following section.
Considering that the central wavelength of Bragg reflection changes with temperature due to thermal expansion, it is evident that keeping a stable temperature is mandatory for achieving a stable CBXFEL output. The usage of two crystals of the above noted thickness increases the robustness of the setup to this point in comparison to the usage of a thinner outcoupling mirror. For comparison, this was discussed in prior publications [12, 13, 23–25]. While it has been discussed to use crystals much thicker $t_C \gg 100\,\mu\mathrm{m}$, the transmission would drop strongly. Besides, it is increasingly more difficult to grow crystals with larger depth without compromising quality. Furthermore, cooled diamonds will be used for the reason of a much increased thermal conductivity [26, 27], while keeping the ratio of excess heat to thermal expansion almost constant [20]. This point will be highlighted at the end of the following section.
For the cooling, a helium pulse tube cooler will be used as described in [28], which is principally able to reach a base temperature $T_B = 30\,\mathrm{K}$. However, the cooling power drops with decreasing the base temperature. At $T_B = 77\,\mathrm{K}$, which is the boiling point of nitrogen, a relatively good compromise between a low and thermally favorable base temperature and an average cooling power of 30 W is obtained [28].

III. DEMONSTRATOR PERFORMANCE

The CBXFEL-demonstrator is planned to work at a fixed photon energy. In the following, the results of the simulations performed for a photon energy of $E_c = 6.95\,\mathrm{keV}$ is presented for the four undulator cells . More details on the simulations are given in Appendix A. $E_c = 6.95\,\mathrm{keV}$ corresponds to the diamond reflection order <4 0 0> and, hence, the most simple <1 0 0> cut direction of diamond. Focal lengths of $f_{\mathrm{US}} = 44\,\mathrm{m}$, equal in both transverse directions, at the upstream retroreflector and $f_{\mathrm{DS}} = 36\,\mathrm{m}$ at the downstream retroreflector are assumed. The axial symmetric focusing strength is introduced by a similar meridonial curvature on both perpendicular mirrors in one retroreflector configuration. The asymmetric focusing between the upstream and downstream retroreflectors is chosen such that the beam waist is at the center of the third undulator cell. However, additional simulations have shown that the focal length is a non-critical parameter, as the CBXFEL remains stable over a wide range $f_{\mathrm{DS}} = f_{\mathrm{US}} \in 30\,\mathrm{m}$ to 90 m, also in symmetric configuration. The simulations are based on a $Q_{\mathrm{bunch}} = 250\,\mathrm{pC}$ electron bunch charge and distributions with a peak current of $\hat{I} \approx 5\,\mathrm{kA}$ as derived in [29]. This is in accordance with the common operation mode of the European XFEL accelerator. Additionally, normal distributed shot to shot variation in some important electron parameters are considered. These shot to shot fluctuations will be referred to as jitter in the following. Specifically, beam energy jitter, electron arrival time jitter, mean position and the arithmetic pointing jitter of

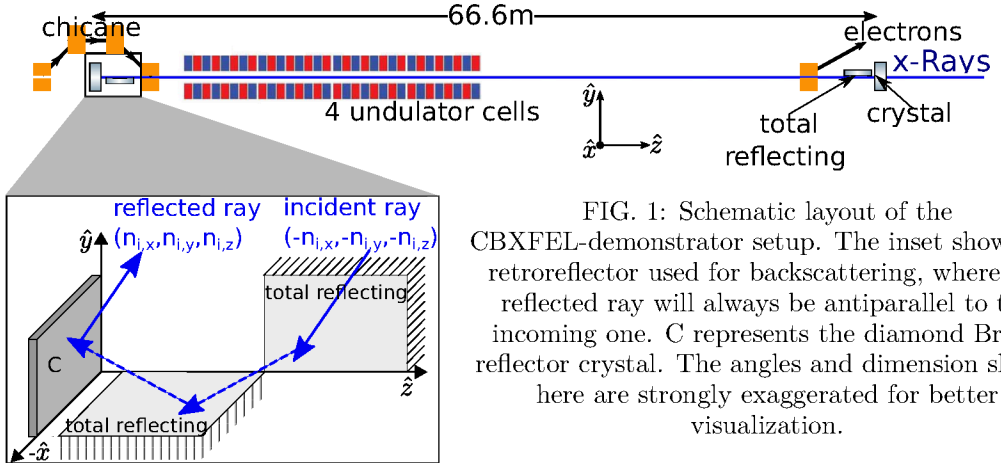

FIG. 1: Schematic layout of the CBXFEL-demonstrator setup. The inset shows the retroreflector used for backscattering, where the reflected ray will always be antiparallel to the incoming one. C represents the diamond Bragg reflector crystal. The angles and dimension shown here are strongly exaggerated for better visualization.

TABLE I: Electron beam parameters (statistical) used for simulation.

Bunch Charge Q_{el}	Electron Energy E_B	Energy Spread σ_{E_B}	Energy Jitter $\sigma_{E_B}^{\text{jit}}$ [a]
250 pC	16 GeV	1.5 MeV	1.6 MeV
bunch length σ_t^{curb}	arrival time jitter$\sigma_{t,\text{arr.}}^{jit}$ [a]	el. position jitter $\sigma_{x,y}^{\text{jit.a}}$	el. pointing jitter $\sigma_{x',y'}^{\text{jit.}}$ [a]
16 fs	20 fs	3 µm	100 nrad

[a] The denoted value expresses the standard deviation of a normal distribution from which the actual error is drawn on a shot to shot basis.

[b] This is computed using the mean absolut deviation $\mathcal{D}_{u,\text{MAD}}$, which is less sensitive to tails in the distribution. It is then transformed into the more common standard deviation $\sigma_u \approx \sqrt{\frac{\pi}{2}}\mathcal{D}_{E_{\text{ph}},\text{MAD}}$.

the electron bunches are considered. The magnitude of the individual jitters are taken from experimental measurements carried out at the actual accelerator. Based on these measurements, the mean position and the mean pointing of the electron bunch fluctuate over a rms width of roughly one tenth of the spatial and angular width of the bunch [30], which amounts to $\sigma_{x,y}^{\text{jit.}}$ =3 µm and $\sigma_{x',y'}^{\text{jit.}}$ = 100 nrad. The energy jitter was measured to fluctuate over one permille from shot to shot [30], which is for the 16 GeV electron beam studied here a total value of $\sigma_{E_B}^{\text{jit.}}$ =1.6 MeV. The arrival time stability of the European XFEL was, based on the very precise timing system, quantified as $\sigma_{t,\text{arr.}}^{jit}$ = 20 fs [31].

To account for misalignment, the downstream diamond mirror is assumed to have an additional fixed tilt error of $\Delta\Theta_x = \Delta\Theta_y$ = 100 nrad, which is a demanding but achievable tolerance. Besides having a finite size of l_M =9 cm, resulting in an projected aperture of size 280 µm × 280 µm at an incidence angle of Θ_{in} =3.1 mrad, the KB mirrors are assumed to have a figure error of σ_h^{rms} =1.5 nm, which is a state of the art value. The mirror profiles are displayed in Fig. 2. Lacking the final mirrors, they were computationally generated using the algorithm by *Hua et al.* [32]. Among ten sets of four mirror profiles each, the ones used for this work yielded intermediate performance and can, hence, be regarded as realistic estimates for actual mirrors.

These parameters as well as the cavity parameters are also displayed in Table I and Table II.

Table III presents characteristic values of the saturated X-ray beam for the specific photon pulse energy of E_c = 6.95 keV. Fig. 3 shows the evaluation of pulse energy vs round trips. The data for table III and Fig. 3 was derived from averaging over 15 individual runs. For the specific simulation framework see Appendix A.

First, the results excluding the impact of the thermal load will be shown. These results highlight the perspective performance of the CBXFEL if the important point of heat load can be controlled. With the parameters under consideration the CBXFEL demonstrator would reach saturation after only about 30 round trips, as evident from Fig. 3 . This is true for both a simulation with the beam jitter and X-ray optics errors discussed above as well as for one without these, with the latter reaching much higher overall pulse energy in the cavity[35]. The number of round trips to saturation is much less than what is normally required for a typical FELO, being on the order of a couple of hundreds (see for example [7]). This is due to the excellent electron beam quality at the EuXFEL leading to a single pass FEL-gain well beyond one, even though only using four undulator cells. Observing the error limits, one can clearly distinguish two regions. The first is the startup or gain regime, where the shot to shot electron fluctuation still strongly influences the gain. This basically increases the number of round trips needed for saturation, leading to high standard deviations for a specific round trip for individual bunch trains. The second is the saturation regime, where the

TABLE II: Cavity and X-ray optics parameters used for simulation.

mirror-mirror distance	crystal material	crystal thickness	cryostat temperature T_C
66.42 m	diamond	100 µm	77 K
focal lengths[a]	projected mirror aperture[b]	downstream mirror tilt	mirror figure error σ_h^{rms}
(37 m and 44 m)	280 µm × 280 µm	$\Delta\Theta_x = \Delta\Theta_y$ =100 nrad	1.5 nm

[a] These are the focal lengths at the downstream (first value) and upstream retroreflector (second value). The values are the same in both transverse planes.
[b] The projected aperture can be easily calculated by the length of the individual KB mirrors times the angle of incidence. As both length and angle of incidence are the same for both KBs at the respective retroreflector, the resulting aperture is quadratic in the transverse domain.

TABLE III: Main parameters of the resulting X-ray pulses in saturation. The errors denote the standard deviation of the shot-to-shot fluctuation in saturation as well as by averaging over 15 individual runs with equal base parameters. For comparison also SASE parameters for the 6.95 keV photon energy and the same electron distribution are appended. These are obtained by simulation (no taper) and scaling to measured energies.

Photon Energy E_{ph} [keV]		6.95	
	before reflection	transmitted	SASE
Pulse Energy Q_{pulse} [mJ]	12.07(3)	0.83(4)	∼3.5 [33]
Bandwidth $\sigma_{E_{\mathrm{ph}}}$[a] [meV]	18.7(1)	87(3)	∼16000
Pulse Length σ_t[a] [fs]	76.6(2)	79(2)	∼11
Time-Bandwidth product $\sigma_t\sigma_\omega$[b]	2.17(1)	10.5(7)	∼280
Gaussian Quality J[c]	10.69(3)	2.8(1)	∼1.1
Peak Brilliance $\mathcal{B}$ [d] [e]	$9.9(1)\times10^{34}$	$5.4(6)\times10^{33}$	$\sim3\times10^{33}$

[a] The bandwidth/duration is computed using the mean absolut deviation $\mathcal{D}_{u,\mathrm{MAD}}$, which is less sensitive to the wide tails in the spectral distribution. It is then transformed into the more common standard deviation $\sigma_u \approx \sqrt{\frac{\pi}{2}}\mathcal{D}_{E_{\mathrm{ph}},\mathrm{MAD}}$.
[b] The time-bandwidth is a simplified means for estimating the occupied volume in the longitudinal domain.
[c] The gaussian quality factor J (see [34]) is, for a transversely coherent beam, a measure invariant under (transverse) linear transformation and an estimate for the volume occupied in the transverse phase space. For an ideal gaussian beam the quality factor has a minimum value of $J = 1$.
[d] #Phot/s/mm^2/mrad^2/0.1%BW
[e] The brilliance is approximated via Eq. (1).

pulse energy does not change from shot to shot. It is evident that the X-ray beam is far more stable than a SASE in saturation, especially if one takes into account the additional need of monochromatization for SASE. This can also be seen in the derived data in Table III, showing some figure of merit parameters highlighting the radiation quality in saturation. Here, one has to differentiate between the energy which is trapped inside the cavity and the one which is actually transmitted.

For the radiation trapped inside the cavity, the pulse energy reaches values even higher than for SASE while having a three orders of magnitude smaller bandwidth. The reason why the brilliance, as a measure of the photon density in the 6D phase space, is only roughly factor 30 better than for SASE is due to the reduction of the transverse quality, as visible from the higher gaussian quality factor J. The gaussian quality factor J (see for example *J. Alda* [34]) is a measure for the volume the photon pulse occupies in the 4D transverse phase space, with a minimum value of $J = 1$ for a gaussian beam. Estimating the brilliance as [36]

$$\mathcal{B} \approx \frac{Q_{\mathrm{pulse}}}{\pi^2\hbar\lambda_0 cJ}\frac{E_{\mathrm{ph},0}}{\sigma_t\sigma_{E_{\mathrm{ph}}}}, \tag{1}$$

the brilliance scales inversely proportional to J. The reduction in J compared to the SASE radiation is caused by the imperfections of the X-ray optics in the cavity, and especially by the figure errors of the X-ray mirrors. Hence, an improvement in the quality of the optics directly translates into an improvement of the CBXFEL photon pulse quality. So, for an actual permanent CBXFEL setup, it would be worthwhile to invest in as perfect optics as possible.

Considering the radiation which is transmitted on a pass to pass basis, the pulse energy in saturation is decreased while the bandwidth is actually increased. While it could be principally possible to couple out the full radiation before reflection by so called cavity-dumping, this would first reduce the pulse frequency by at least a factor of 30 (the number of bunches to reach saturation) and second, would require more involved components and therefore add complexity to the setup (see, for example, [37] or a list of outcoupling mechanisms in [20, ch. 2.4]). The lat-

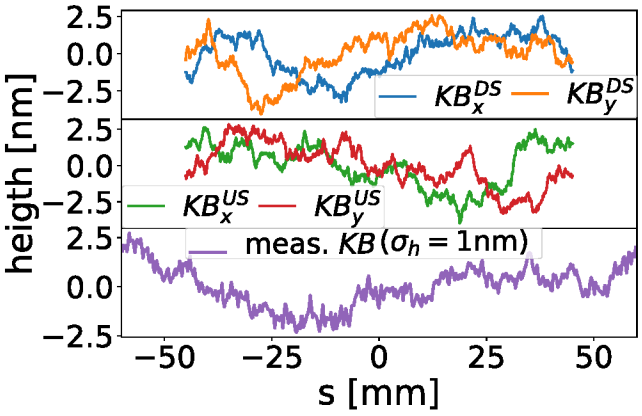

FIG. 2: Numerically generated surface profiles with rms profile error of σ_h =1.5 nm (top panel corresponding to the downstream Kirckpatrick-Baez (KB) mirrors and middle panel to the upstream ones). The subscripts x and y symbolize if the long axis of the mirrors projects on the x or y axis of the beam. For comparison a mirror actually used and measured at the European XFEL is shown in the bottom panel. It has slightly better rms error compared to the numerically generated ones. For better emphasizes on the figure error, the deliberately introduced surface curvature is subtracted for each mirror.

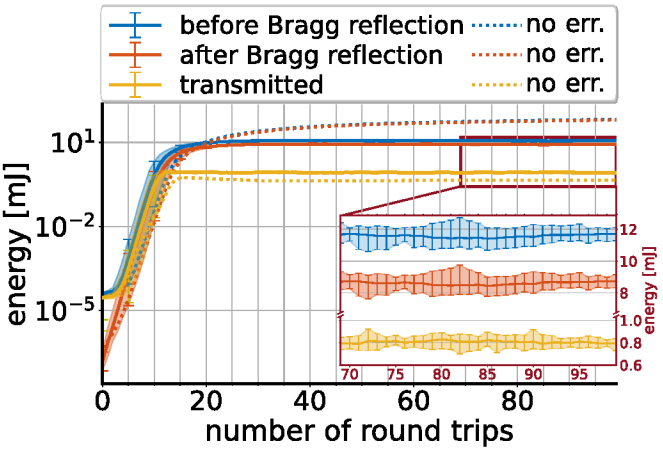

FIG. 3: Evolution of pulse energy for a photon energy of $E_c = 6.95$ keV. The larger plot shows the full evolution in logarithmic scale while the inset shows the pulse energy after saturation in linear scale. Please note the broken ordinate in the inset to better emphasize the transmitted pulse energy. The data is based on averaging 15 individual runs, with the solid lines representing the ensemble average and the shaded area the full range of pulse energies for the specific shot. The dotted lines in the main plot represent the ensemble average of twelve runs without any jitter or tilt error introduced. The blue and orange curve at the first round trips are unrealistically low as they are based on a much reduced bandwidth compared to the full SASE spectrum.

ter point contradicts the intention to keep it as simple as possible.

In the following, it shall be described how radiation can actually be transmitted on a pass to pass basis using two thick crystals with a central transmissibility of roughly zero. The mechanism makes use of the high single pass gain of the setup. This leads to a considerable amount of newly generated X-ray pulse energy at every roundtrip which is roughly the saturation energy also given in untapered SASE. A fraction of this energy will be distributed to the spectral region outside the reflection bandwidth of the crystal. This can be seen in Fig. 4(a) for the blue curve presenting the spectrum of the X-ray pulse in saturation before reflection. While there is a dominant spectral peak inside the reflection bandwidth as expected, one can also see comparably low magnitude but wide pedestals outside in the logarithmic scale inset to Fig. 4(a). As is evident from the yellow curve representing the downstream crystal transmission in Fig. 4(a), the dominant peak will be nearly totally reflected while a strong fraction of the pedestals will actually be transmitted. The resulting spectrum is presented in Fig. 4(b). The magnitude of the pedestals correlates strongly with the temporal duration of the electron bunches, with shorter electron bunches generating larger pedestals in the FEL radiation. For the $Q_{\text{bunch}} = 250$ pC electron bunches under consideration their temporal width does not fully support the low spectral width of the crystal reflection due to the limits of Fourier transformation. Therefore, the newly generated radiation will always have a higher spectral bandwidth compared to the seed bandwidth which is given by the reflection width. While this limits the seeding efficiency, it increases the fraction of transmitted energy. It is also worth noting that the transmitted pulse is newly generated at every round trip. This is contrary to the classic low gain FELO case, in which a low percentage of the full spectrum, which is averaged over many round trips, is coupled out at every turn.

In the inset of Fig. 4(b) a comparison to SASE spectra referring to the numbers in Table III is displayed, clearly exhibiting orders of magnitude higher spectral flux of the transmitted CBXFEL pulse. In Fig. 4(c) the corresponding intensity profile is shown. The comparison to SASE in the inset exhibits a higher intensity of the short pulse SASE. On the other hand, the CBXFEL pulse peaks at much higher spectral energy densities than the SASE. While the transmitted radiation does not undergo any averaging over many round trips, it still is very stable. This is evident from both the standard deviations in Table III as the shaded areas in the figures, representing the rms range over 15 independent bunch trains and 100 bunches in saturation each. This follows from the very strong, stable and monochromatic seed which leads to reproducible single pass gain and strong gain guiding.

Both spectrum in Fig. 4(b) and intensity profile in Fig. 4(c) clearly are no single peak distributions anymore

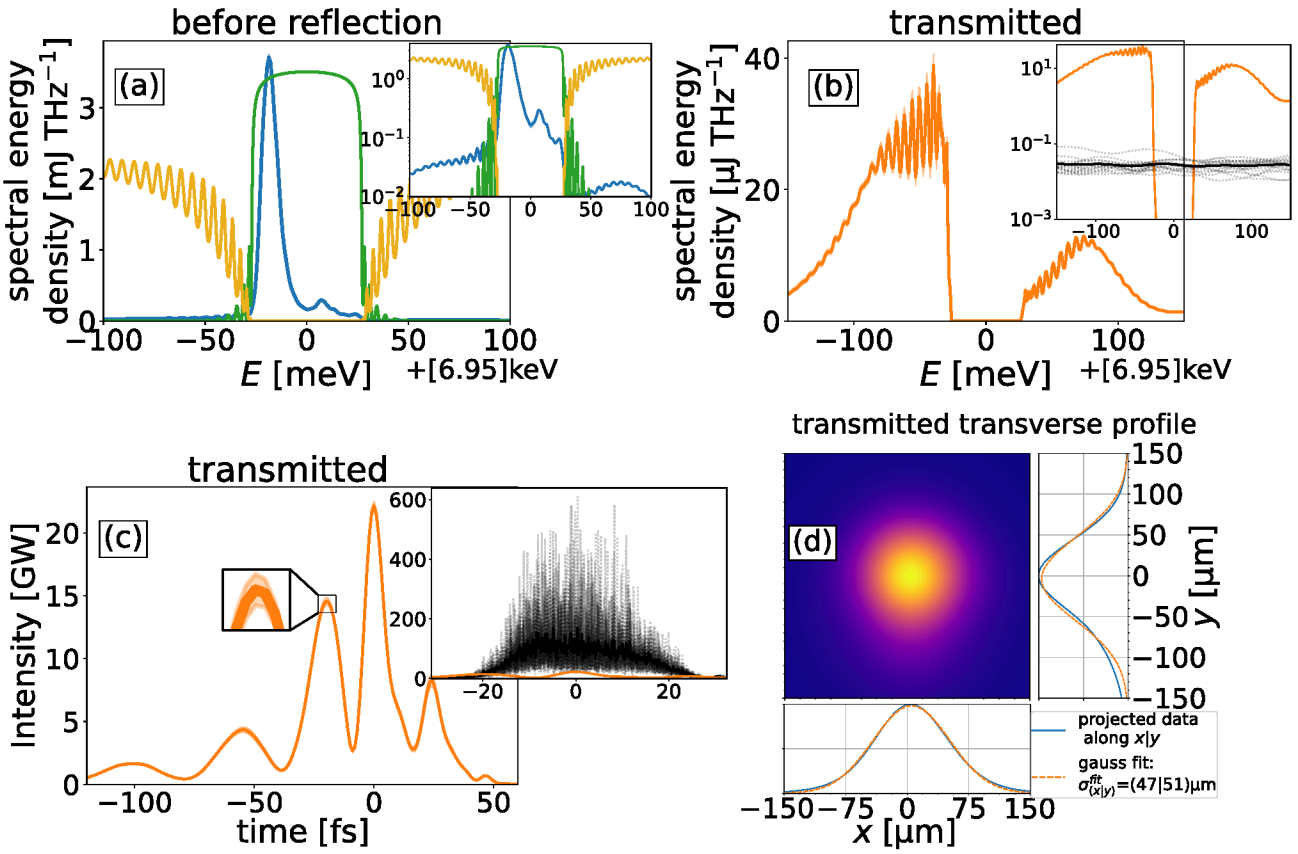

FIG. 4: (a) shows the transversely integrated longitudinal spectra of the X-ray pulse at $E_c = 6.95\,\mathrm{keV}$ directly after the undulator (blue). (a) also shows the cumulative reflection (green) of both diamond mirrors and the transmissivity (yellow) of the downstream one. The inset is the same graph with logarithmic ordinate to better highlight the pulse tail outside the reflection bandwidth. (b) displays the transversely integrated longitudinal spectra of the transmitted pulse (orange). In the inset also the SASE spectra of 15 statistical runs in light gray and their ensemble average in black are plotted on a logarithmic scale for comparison. (c) shows the transversely integrated intensity profile in time domain, where the orange curve is the average over 100 round trips in saturation and fifteen consecutive runs. The width of the line corresponds to the respective rms range. As the relative variation is very small, for better visualization the inset in (c) on the left zooms in such a widening. The same rms-widening is existent in (a) and (b), but likewise very small. The inset in (c) on the right displays the comparison to 15 SASE runs. (d) presents the transverse projection of the transmitted pulse, which is on the same scale as the one trapped in the cavity, but less affected by wavefront distortions.

and therefore also occupy a larger volume in the longitudinal phase space compared to the circulating pulse (see Table III). This is caused by the time-frequency correlation induced by the crystal transmission, especially near the edges of the reflection curve. Furthermore, one might expect a transverse-longitudinal correlation of the transmitted pulses [38] and therefore a misshaped transverse profile corresponding to the hole in the transmitted spectrum. As evident from the transverse profile presented in Fig. 4(d), this is not the case. Actually, the transmitted profile has a Gaussian quality factor $M^2 = 2.8(1)$ [34] much better than the trapped radiation pulse. This is due to two reasons. First, the very low spectral width of the hole whose missing contribution to the transverse profile basically gets washed out. And second, due to the transmitted radiation being nearly completely based on the radiation newly generated in the undulator cells at each roundtrip, which are subject to strong gain guiding, the negative impact of the X-ray optics imperfections are partially washed out.

With respect to the actual CBXFEL demonstrator experiment, the transmitted energy and especially the evolution of the spectral peak with the number of roundtrips will be very well measurable using the fast X-ray spectrometer *HIREX* [39] at the SASE1 beamline. After only roughly five to ten round trips the development of a distinct spectral peak shall be visible in the stochastically fluctuating noisy synchrotron radiation dominated background. As sketched in Fig. 5, the growth of this peak can than be tracked at a much earlier number of round trips than the actual growth of the transmitted pulse energy. This would already be sufficient to prove the work-

ing concept of a CBXFEL.

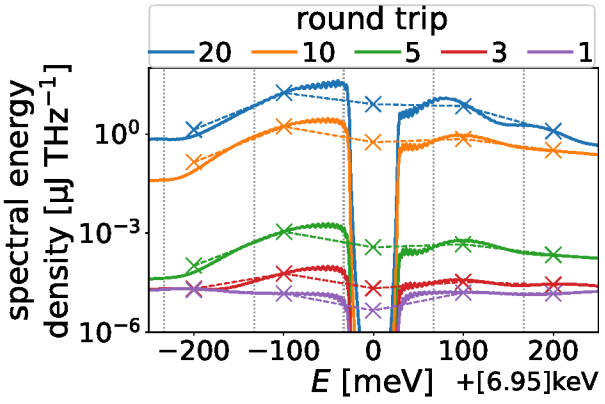

FIG. 5: Evolution of the transmitted spectral energy density versus number of round trips in logarithmic scale. The spectra are averaged over ten individual bunch trains. The dotted, marked lines show the spectrum which would be observable with an idealized spectrometer with a resolution of ΔE=100 meV and perfectly centered on $E = E_c$ =6.95 keV. Both in the high resolution as in the binned spectrometer data one can already see a significant rise in the spectral energy density at the third round trip.

IV. IMPACT OF THERMAL LOAD

Up to now, the prominent influence of thermal load on the CBXFEL process hrings abouas been neglected in this paper. Hence, the results so far represent an estimate for the performance principle reachable by this setup, for the idealized case the thermal load could be handled. However, at the very high pulse energies and small footprints of the X-ray pulse at the diamond as considered here, the heat load deposited in the crystals has a very strong impact on the CBXFEL process. As will be discussed below, this is especially true for crystals at room temperature, limiting the maximum pulse energies to only $Q_{\text{pulse}}^{\text{max}}$ ≈100 µJ, which further exhibit pronounced fluctuations. Yet, also with cooled diamonds the CBXFEL will become unstable, however reaching much higher maximum pulse energies $Q_{\text{pulse}}^{\text{max}}$ ≈3 mJ.
Upper statement is true even if ignoring the very important, but numerically too expensive, dynamic elastic answer of the crystal. This dynamic response adds locally varying elastic waves and, hence, strain to the crystal, which is in approximation independent of crystal temperature. These elastic waves both reduce the spectral reflection efficiency and add wavefront distortions to the reflected X-ray beam. An overview of the impact of this involved effect is given in [40] and [41]. For the results presented here, only the quasistatic thermal expansion at the arrival of the subsequent X-ray pulse, caused by the local residual heat in the crystal, is considered.
In Fig. 6 the pulse energy evolution (top row) in conjunction with the temperature (middle row) at the time of arrival of the (next) X-ray pulse are displayed. Also, the relative losses $\mathcal{L} = \Delta Q/Q_{\text{Und}} \leq 1$ are shown (bottom row), where Q_{Und} is the pulse energy directly after the undulator (the blue line in Fig. 6[(top)]). The losses under consideration are the losses caused by the cut-off at the finite size apertures introduced by the upstream and downstream KB mirrors, the losses caused by the transmission and absorption at the downstream and upstream crystals and the sum of all losses in the cavity. ΔQ is the total energy loss caused by the respective loss channel. The left column in Fig. 6 refers to the crystals without active cooling (T_{base} = 300 K) and the right column to crystals cooled to T_{base} = 77 K.
The underlying simulation is based on the same parameters as for Table III and Fig. 3, but including the thermal response as described above and in more detail in the Appendix **A**. It is evident that the thermal impact of the X-rays on both cooled as non-cooled crystals strongly destabilizes the CBXFEL, with the pulse energy and, foremost, the downstream crystal temperature being strongly correlated. Both energy as temperature evolution curves show a very pronounced beat, with the downstream crystal temperature rising as much as tremendous $T_{\text{ds}}^{\text{max}}$ ≈580 K for the T_{base} = 77 K case. For the room temperature case the rise in crystal temperature peaks at a much lower $T_{\text{ds}}^{\text{max}}$ ≈310 K. This can be easily traced back to much lower maximum pulse energy of $Q_{\text{pulse}}^{\text{max}}$ ≈100 µJ for the room temperature crystals compared to $Q_{\text{pulse}}^{\text{max}}$ ≈3 mJ at the T_{base} = 77 K case, which correspond to a much lower maximally absorbed heat energy (purple line in Fig. 6[(top)]). This one order of magnitude difference in maximum pulse energy actually highlights the importance of the cooling of the crystal.
As can be deduced from the evolution of the cavity losses in Fig. 6[(bottom)]), the reason for the loss of seeding is quite different for the two cases. For the room temperature case, it is caused by a massive rise in aperture losses due to a widening of the X-ray pulse on the KB mirrors. This pulse widening can be backtracked to a defocussing by the non-homogenously heated crystals which develop a pronounced heat bump. The defocussing caused by a temperature bump is a well known problem, for example also discussed with respect to the efficiency of self seeding [42]. For the T_{base} = 77 K case, the much higher thermal diffusivity at low crystal temperatures causes a much more homogenous heat distribution at arrival of next pulse at the tens of micrometer scale of the X-ray beam. This causes a much slower rise of the aperture losses. Actually, in Fig. 6[(bottom)] we also see a strong rise in aperture losses, but this is one round trip after the seeding was already lost. This loss of seeding can be totally attributed to a strong rise in spectral losses at the crystals for the cooled crystals, which will be explained

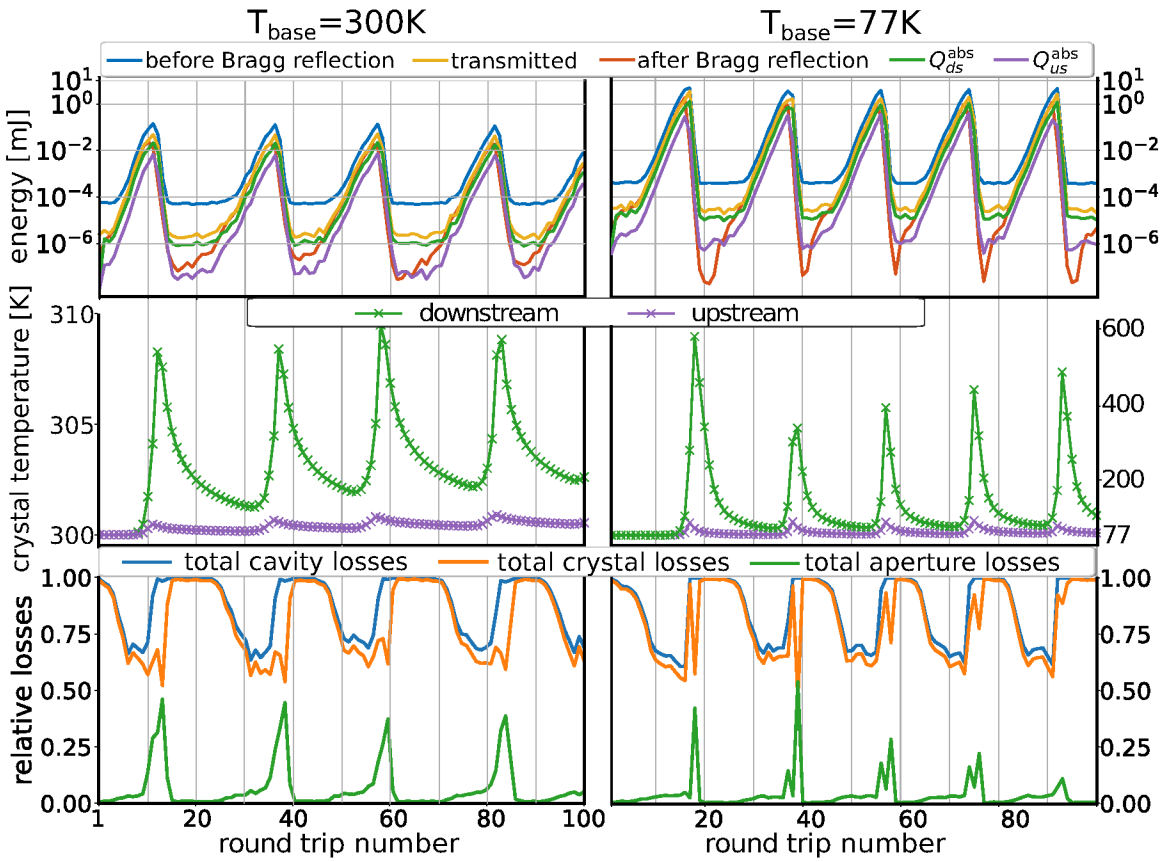

FIG. 6: Evolution of pulse energy (upper row) under influence of thermal load, temperature of the crystal (middle row) and relative cavity losses $\mathcal{L} = \Delta Q/Q_{\mathrm{Und}}$, where Q_{Und} is similar to the blue line in the top row plot, with subsequent round-trips. The crystal temperature is evaluated at the center of the incoming X-ray beam. The left column refers to a crystal base temperature of $T_{\mathrm{base}} = 300\,\mathrm{K}$ (room temperature) and the right column to the crystal cooled to $T_{\mathrm{base}} = 77\,\mathrm{K}$. The losses in the bottom row refer to the sum of all losses in the cavity (blue line), the sum of absorption and transmission losses at both the crystals (orange line) and the cut-off losses introduced by the finite size of the KB-mirrors (green line). For both temperatures energy and temperature strongly correlate and show a highly unstable operation. Actually, the maxima in pulse energy and temperature are shifted by one round trip, as at the round trip the pulse energy drops off, due to a missing overlap of spectral reflection and incident radiation (see Fig. 7), a higher fraction of incident radiation gets absorbed, leading to a very strong temperature rise. For the losses, one can see an anti-correlation between the aperture and crystal losses. As all the summed losses have to be ≤ 1, a particularly strong rise in one of the loss channels causes a relatively smaller loss in the others. This does, however, not mean an actual drop of pulse energy loss in total number. It is noteworthy that for the room temperature case one can first see a strong rise in aperture losses, causing the break off of the CBXFEL seeding, and only afterwards a rise in spectral losses. Latter is due to the loss of the seeding, causing a much higher fraction of transmission. For the cooled crystal case, on the other hand, the drop off is caused by a strong rise in spectral losses which is then followed by a rise in aperture losses at the next round trip.

in more detail below.

Fig. 7 depicts the spectra of the X-ray pulse incident on the downstream crystal in conjunction with the reflection curves of the downstream crystal for the round trips around a seeding loss at round trip 92. It is evident from Fig. 7 that with increasing round trips and, hence, increasing pulse energy, the reflection curve of the downstream crystal (green dashed curve) shifts with respect to the central reflection photon energy. As the upstream crystal only slightly heats up and, hence, does not exhibit such a shift, a reduction of the cumulative reflection width occurs. This is one causes for the increase in reflection losses. However, the loss in seeding is not due to a miss in overlap of the two reflection curves but due to a too strong heating of the downstream crystal, which shifts the downstream reflection curve completely out of the spectrum of the incident radiation. Hence, the process can not be compensated by matching the downstream and upstream heating[43].

As can be seen both from the rising fraction of the red

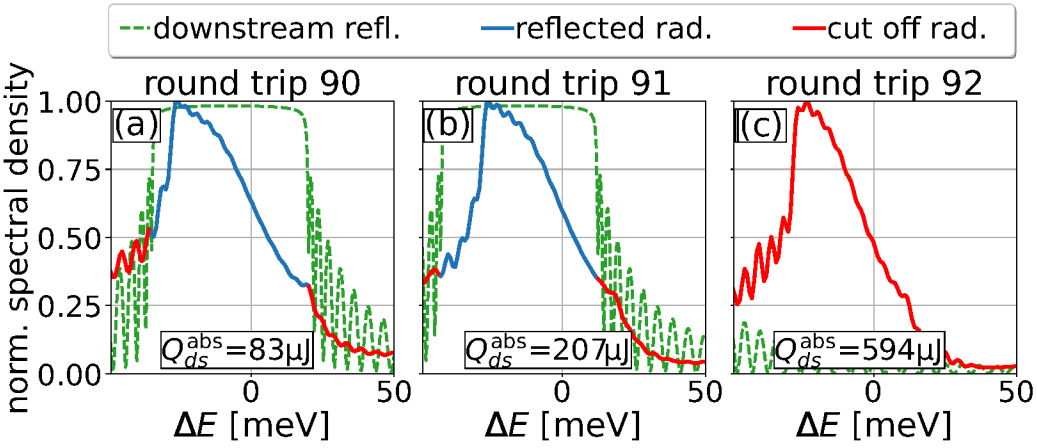

FIG. 7: Spectra for the T_{base}=77 K case after the undulator and before reflection (blue and red solid) together with the spectral reflection curves of the downstream crystal (green dashed), for different round trips around the maximum pulse energy (round trip 92). The blue curve highlights the fraction of the incident radiation which will be nearly completely reflected by the downstream crystal, while the red curve highlights the fraction of the incident radiation which gets cut off, or rather transmitted, at the downstream mirror and is, consequently, more strongly absorbed. This cut-off fraction increases towards round trip 92, which is also highlighted by the increasing amount of absorbed heat energy at the downstream crystal Q_{ds}^{abs} shown at the bottom of each plot.

cut-off line in Fig. 7 as well as the evolution of the reflection losses in Fig. 6(left, bottom), the process of the reflection shift is strongly non-linear. This is due to three, coupled, reasons. The first is simply the exponential rise in pulse energy, coming with an exponential rise in heat load. The second is non-linearity of the heat conduction process. At increasing heat load the diffusion process actually slows down with the strong decrease in the thermal diffusivity D_{th}, causing an even stronger temperature rise. The diffusion is additionally slowed by the remaining, spread out heat of the prior round trips, which decrease the local curvature $\nabla^2 T$. The resulting decrease in thermalization efficiency causes an exponentially growing impact of the crystal heating on the lattice expansion and, hence, the diffraction process. This also leads to a growing difference in the temperature of the both crystals.

Finally, as depicted in Fig. 7, the impact of the thermal load on the downstream crystal get further amplified by the fact that the shift in the spectral reflection curve at higher temperatures actually leads to a higher mean penetration depth of the incident X-rays. As the absorption coefficient remains constant, a larger interaction volume in the crystal corresponds to a larger total absorption of the pulse. This then induces a stronger heating. Foremost this effect causes the almost exponential growth in temperature and, likewise reflection losses, near the maxima in pulse energy. This exponential growth in temperature is also the reason why the heat bump effect of the crystals only becomes important at the time the seeding is already lost due to the spectral shift of the reflection curves.

It should be noted that at the exact round trip the pulse energy after reflection considerably drops of, nearly the entirety of the radiation incident on the downstream crystal is transmitted. This can be framed as a *passively cavity-dumped* system in relation to the active cavity dumping known from high power optical lasers [44, Ch. 9.5] or also discussed for CBXFELs [37]. The cavity dumping occurs with a rather stable periodicity with the crystal quickly cooling down and then heating up again between two cavity dumps[45]. For the exemplary cavity dump at round trip 92, the transmitted pulse reaches a pulse energy of $Q_{\text{tr}}^{\text{rn=92}}$ ≈1.56 mJ at a bandwidth of only $\sigma_{E_{\text{ph}}}$≈55 meV in combination with a rather small time-bandwidth product of $t\omega$ ≈10. However, the strongly heated downstream crystal at the moment of the cavity dump also imprints its distortion on the wavefront of transmitted pulse, causing an increased gaussian $J \approx 194$ and, correspondingly, reduced peak brilliance of only $\mathcal{B}$=1.5×10^{32} #Phot/s/mm^2/mrad^2/0.1%BW.This is highlighted in Fig. 8. Yet, these transmitted pulses may be very interesting for some special experiments requiring very high spectral energy densities. Also, they are interesting for analysis, as they carry a lot of information regarding the heating of the crystals as well as information of the radiation stored in the X-ray cavity.

V. CONCLUSIONS

A setup for the first ever proof of concept X-ray free-electron laser oscillator for the European XFEL facility is presented. This setup can potentially produce very intense X-ray pulses at a fixed wavelength with unparalleled spectral energy density. A simple outcoupling mechanism is proposed which uses the transmissivity of 100 μmthick crystals outside the reflection width provid-

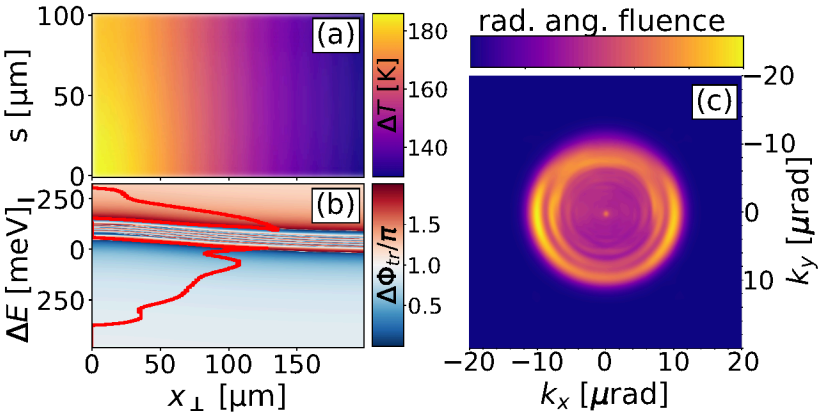

FIG. 8: Distribution of the downstream crystal temperature $\Delta T = T_c - T_{c,\mathrm{base}}$(a) at the arrival of the X-ray pulse at the 92nd round trip. This temperature distribution brings a spatially varying, transmission induced phase shift $\Delta\Phi_{\mathrm{tr}} = \mathrm{phase}\,(t_{00})$(b). In (b) also the 99 % contour of the transmitted pulse is plotted, visualizing which parts of it are subject to a spatially varying phase shift, which is consequently deforming the pulse wavefront. Latter is highlighted by the radiant angular fluence in the angular domain(c).

ing more stability with respect to the megahertz repetition rate X-ray induced heating of the diamond crystals. By cryogenically cooling the diamonds to liquid nitrogen temperature, the impact of the crystals thermal response is further reduced.
However, even with these measures introduced the tens of micrometer wide, very intense X-ray pulses circulating in the cavity will inhibit the CBXFEL demonstrator to reach a stable operational state. In principle, there are methods to further stabilize the CBXFEL. These include FEL based concepts to, potentially adaptively, reduce the gain and thereby the maximum pulse energy; X-ray optics based schemes to reduce the cavity quality factor; and/or crystal geometry based schemes to increase its resistance to heat load. Yet, they all have in common that they add major complexity to the experimental setup and their chance of success is dependent on the accuracy of the involved modeling of the thermal response. As the principle goal of the experiment to proof seeding is not impeded by the described effects, these stabilization schemes will not be foreseen for the initial CBXFEL demonstrator experiment. Additionally, the results of the demonstrator experiment can be used to better understand the thermal response related effects and, hence, develop countermeasures more efficiently. Enhancements in the outcoupling mechanism to further improve the X-ray quality are also planned.

ACKNOWLEDGMENTS

This work was funded by the Federal Ministry of Education and Research under FKZ 05K16GU4, by the European XFEL GmbH and by Deutsches Elektronen-Synchrotron (DESY). The numerical results were obtained using the Maxwell computational resources operated at Deutsches Elektronen-Synchrotron (DESY), Hamburg, Germany. I am happy for suggestions regarding the acknowledgements.

Appendix A: Simulation framework

The simulations framework used to produce the discussed data is explained in detail in the PhD thesis by *P. Rauer* [20]. Also, a more compact publication on this topic will soon follow. Here, only the basics of it shall be sketched.
The framework consists of two to three subprograms, depending if the thermal response shall be included or not. The FEL simulation is done by using the well known *Genesis-1.3* FEL code [46, 47]. The radiation produced by Genesis is then read in by the *parallel X-ray Cavity Propagator* (pXCP) wavefront propagation code especially developed for this project which is propagating the X-ray radiation through the optical cavity. The code is heavily parallelized using distributed *Massage Passing Interface* (MPI) parallelization for use at computing clusters. The code first transforms the radiation into the frequency domain using the *FFTW* library [48] and then propagates each frequency slice independently using the Fourier optics approach [49, 50]. Performing the propagation in the frequency domain is natural for this problem as the interaction with the crystal mirrors is easiest to model in the frequency domain. The interaction with the crystal mirrors is based on a simple 3D $k-f$—space two beam approach [38] taking into account the actual temperature dependent data and the susceptibilities taken from the *xraylib* library [51, 52]. For simulations taking into account the thermal load on the crystals and therefore spatially distorted crystal a 1D strained layer two beam approach [53] is chosen. This is done for each point of the radiation grid in positional space. This approach is possible for the symmetric case close to backscattering discussed here, as the radiation only perceives the strain component along the surface normal [54]. For incident angles deviating from 90° a more time consuming approach is necessary, for example the one derived in [55]. If no heating is considered, the radiation data after propagation is saved to disk to be read in again by *Genesis1.3* for the next round trip. Dependent on the resonant wavelength a full scale simulations takes roughly one to four hours on 400 cores. If thermal load is considered an additional step is necessary. For this the incident X-ray

pulse fractionally absorbed by the crystal is sampled in the propagation code and read in by the finite element software *Comsol Multiphysics®*. Assuming a cylindrically symmetric 2D geometry for faster computation, the heat distribution is simulated using Fourier's heat law taking into account the strong nonlinearity especially at low temperatures. Additionally, boundary scattering assuming diffusive boundaries limiting the heat diffusion is included by using a reduced effectively anisotropic thermal conductivity [56–58]. The crystal temperature after one round trip time is then written out. After the Genesis-1.3 run this temperature file is then used by the wavefront propagation code to calculate an updated crystal reflectivity for the propagation of the subsequent pulse. Then the procedure repeats. The remaining temperature in the crystal is saved in between the subsequent pulses, so that a stacking of the heat remaining in the region of interest can be accounted for.

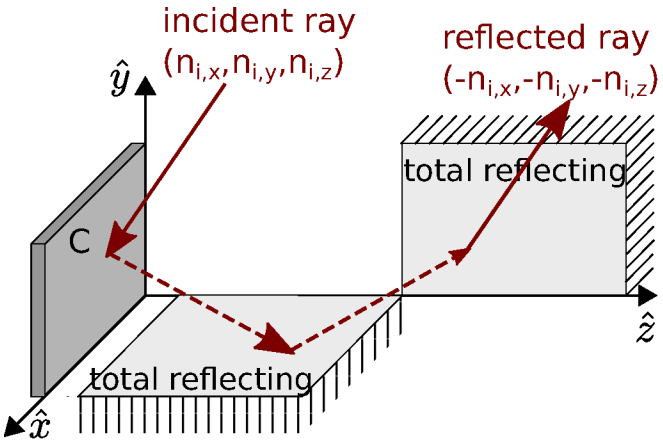

FIG. 9: Schematics of a 3D retroreflector, where three mirrors (two grazing incidence, total reflecting ones and one crystal (C) mirror) are assembled perpendicular to each other. In this way, the reflected ray will always be antiparallel to the incoming one, given it remains in the angular acceptance of the individual mirrors. The sketched angles are strongly exaggerated compared to the real case for better visual representation.

Appendix B: Retroreflector

In Fig. 9 a retroreflecting setup is sketched, consisting of two total reflecting, grazing incidence mirrors and one crystal mirror. By aligning these mirrors perfectly perpendicular to each other, the rays reflected by this setup will always be perfectly antiparallel to the incoming ones. Using the general form of the reflection matrix $\mathbb{S}_i = \mathbb{1} - 2\hat{\boldsymbol{n}}_i\hat{\boldsymbol{n}}_i^T$, where $\hat{\boldsymbol{n}}_i$ is the unit vector normal of the reflecting plane, and noting that $\hat{\boldsymbol{n}}_i\hat{\boldsymbol{n}}_{j\neq i} = 0$ for three perpendicular mirrors i, j, then $\mathbb{S}_{\text{ass.}} = \mathbb{S}_3\mathbb{S}_2\mathbb{S}_1 = -\mathbb{1}$, proving above statement. It directly follows that any incoming ray with wavevector $\boldsymbol{k}_{in}$ will be transformed to $\boldsymbol{k}_{out} = \mathbb{S}_{\text{ass.}}\boldsymbol{k}_{in} = -\boldsymbol{k}_{in}$. Hence, as noted above, the reflected ray will always be antiparallel to the incoming one, no matter the initial orientation. The same also holds for the three perpendicular mirror orientations of the demonstrator setup

$$\hat{\boldsymbol{n}}_{M1}^{(m)} = \begin{pmatrix} \cos(\alpha) \\ \sin(\alpha) \\ 0 \end{pmatrix}, \qquad \hat{\boldsymbol{n}}_{M2}^{(m)} = \begin{pmatrix} -\sin(\alpha) \\ \cos(\alpha) \\ 0 \end{pmatrix}, \quad \text{(B1)}$$

$$\hat{\boldsymbol{n}}_{C}^{(m)} = \begin{pmatrix} 0 \\ 0 \\ -1 \end{pmatrix},$$

where $M1$ and $M2$ refer to the total reflecting mirrors, C to the crystal mirror and α is an angle noting the orientation of the total reflecting mirrors with respect to the crystal mirror[59]. The use of these orientations can decouple the entire setup from outer vibrations, meaning variations in the incoming wave vector $\boldsymbol{k}_{in} = \boldsymbol{k}_0 + \Delta\Theta\boldsymbol{n}_\perp$, with $\boldsymbol{k}_0$ being a nominal orientation, which is reflected back to itself, $\boldsymbol{n}_\perp \perp \boldsymbol{k}_0$, and $\Delta\Theta$ is an arbitrary angular perturbation. This is unlike the action of a single mirror, for which the reflected ray $\boldsymbol{k}_{out} = \mathbb{S}_{\text{single}}\boldsymbol{k}_{in}$ will form an angle $\measuredangle(\boldsymbol{k}_{in}, \boldsymbol{k}_{out}) \approx \pi - 2\Delta\Theta$ with the incoming one. However, it should be emphasized, that it does not decouple against the motions of a single mirror inside the setup, as this breaks the perpendicularity of the system.

The above assumption about perfectly perpendicular mirror orientations are idealistic. It will be shown, however, that also under influence of a *dyadic error* $\Delta\alpha$, meaning an angular shift away from the perpendicular orientation, the tolerance towards angular variation of $\boldsymbol{k}_{in}$ can be significantly enhanced.
For the derivation it will be assumed, without loss of generality, that the dyadic error will be present in the orientation of the second total reflecting mirror

$$\begin{aligned} \boldsymbol{n}'_{M2} &= \begin{pmatrix} \sin(\alpha+\Delta\alpha) \\ -\cos(\alpha+\Delta\alpha) \\ 0 \end{pmatrix} \\ &\approx \begin{pmatrix} \sin(\alpha) \\ -\cos(\alpha) \\ 0 \end{pmatrix} + \Delta\alpha \begin{pmatrix} \cos(\alpha) \\ \sin(\alpha) \\ 0 \end{pmatrix} \\ &= \boldsymbol{n}_{M2} + \Delta\alpha\boldsymbol{n}_{M1}, \end{aligned}$$

which gives a reflection matrix of

$$\mathbb{S}'_{M2} = \approx \mathbb{S}_{M2} + 2\Delta\alpha \begin{pmatrix} \sin(2\alpha) & \cos(2\alpha) & 0 \\ \cos(2\alpha) & \sin(2\alpha) & 0 \\ 0 & 0 & 0 \end{pmatrix}.$$

This error in M2 can be easily transformed into an error in any of the other mirrors by simple matter of unitary rotation. For above equations, it has been approximated that $(\Delta\alpha)^2 \approx 0$[60]. It can be generally shown, that the product of any three reflection matrices $\mathbb{S}_{\text{ass.}}$, no matter

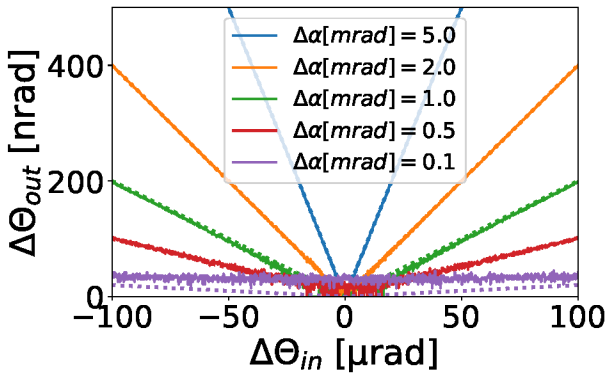

FIG. 10: Influence of the diadic error on the retroreflector compensation. The solid lines correspond to numerical vector analysis, where the orientation of the crystal mirror was tuned such that the beam $\boldsymbol{k}_0$ coinciding with the undulator axis gets reflected back to itself after total reflection and would make an angle of $\Theta_i = 3.1\,\mathrm{mrad}$ with both total reflecting mirrors after reflection at the crystal for the case of $\Delta\alpha = 0$. The dashed lines correspond to the approximation (B2). The agreement is good, except for $\Delta\alpha$ =0.1 mrad, where the numeric results becomes very noisy due to rounding errors.

how oriented they may be, has one specific eigenvalue of $A = -1$ [61, ch.2.10.1][62]. This means, that the corresponding eigenvector $\boldsymbol{k}_0$ will return antiparallel to itself after reflection. For the present set of reflection matrices $\mathbb{S}_{\text{ass.}} = \mathbb{S}'_{M2}\mathbb{S}_{M1}\mathbb{S}_C$, $\boldsymbol{k}_0 = (0, 0, 1)$. However, the actual $\boldsymbol{k}_0$, corresponding to an eigenvalue of -1, can be set by appropriately adjusting the orientation of the crystal mirror. The actual rotation for doing so is rather complicatedly dependent on $\alpha, \Delta\alpha$ and the desired $\boldsymbol{k}_0$. It will usually be numerically set such that $\boldsymbol{k}_0$ becomes equal to the undulator axis:

$$\boldsymbol{k}_0 = \begin{pmatrix} -\cos(P)\sin(R) \\ \sin(P) \\ -\cos(P)\cos(R) \end{pmatrix},$$

where P refers to rotation of the mirrors around the deflection directions of the electrons in a planar undulator and R to the rotation around the magnetic field direction.
Now assuming an incoming vector

$$\boldsymbol{k}_{in} = \boldsymbol{k}_0 + \Delta\Theta\hat{x},$$

which is the same as assuming a tilt of the mirror in the roll angle by $\Delta R = \Delta\Theta$, this becomes

$$\boldsymbol{k}_{out} = \mathbb{S}'_{\mathbf{ass.}}\boldsymbol{k}_{in} \approx -\boldsymbol{k}_{in} - \begin{pmatrix} 0 \\ 2\Delta\alpha\Delta\Theta \\ 0 \end{pmatrix}.$$

For the angular 'error' after reflection, which is defined as the angle between the actual reflected ray and the ideally reflected ray $\Delta\Theta_{out} = \measuredangle(-\boldsymbol{k}_{in}, \boldsymbol{k}_{out})$, one then calculates

$$\begin{aligned} \Delta\Theta_{out} &= \cos^{-1}\left(\frac{-\boldsymbol{k}_{in}\cdot\boldsymbol{k}_{out}}{|\boldsymbol{k}_{in}||\boldsymbol{k}_{out}|}\right) \\ &\approx \cos^{-1}\left(\frac{1}{\sqrt{1+(2\Delta\alpha\Delta\Theta)^2}}\right) \approx 2\Delta\Theta\Delta\alpha, \end{aligned} \tag{B2}$$

where again it was approximated that $\Delta\alpha^2 \approx 0$. This means that a variation of the incoming radiation beam with respect to the mirror assembly can be compensated by roughly a factor $2\Delta\alpha$. Assuming a feasibility of the the dyadic error on the order $\Delta\alpha \tilde{<} 2\,\mathrm{mrad}$, as told by commercial manufacturers, a $\tilde{<} 4E-3$ reduction in angular error can be achieved. In Fig. 10 the angular error $\Delta\Theta_{out}$ is plotted in dependence of the angular variation $\Delta\Theta_{in}$ with respect to the eigenvector $\boldsymbol{k}_0$. The solid lines correspond to numerical vector analysis of a more general mirror orientation and the dashed lines to the equation (B2). Both curves agree very well, showing the reliability of approximation (B2).

[1] Z. Huang and K.-J. Kim, Review of x-ray free-electron laser theory, Physical Review Special Topics - Accelerators and Beams **10**, 10.1103/physrevstab.10.034801 (2007).

[2] J. Amann, W. Berg, V. Blank, F.-J. Decker, Y. Ding, P. Emma, Y. Feng, J. Frisch, D. Fritz, J. Hastings, Z. Huang, J. Krzywinski, R. Lindberg, H. Loos, A. Lutman, H.-D. Nuhn, D. Ratner, J. Rzepiela, D. Shu, Y. Shvyd'ko, S. Spampinati, S. Stoupin, S. Terentyev, E. Trakhtenberg, D. Walz, J. Welch, J. Wu, A. Zholents, and D. Zhu, Demonstration of self-seeding in a hard-x-ray free-electron laser, Nature Photonics **6**, 693 (2012).

[3] I. Inoue, T. Osaka, T. Hara, T. Tanaka, T. Inagaki, T. Fukui, S. Goto, Y. Inubushi, H. Kimura, R. Kinjo, H. Ohashi, K. Togawa, K. Tono, M. Yamaga, H. Tanaka, T. Ishikawa, and M. Yabashi, Generation of narrow-band x-ray free-electron laser via reflection self-seeding, Nature Photonics **13**, 319 (2019).

[4] C.-K. Min, I. Nam, H. Yang, G. Kim, C. H. Shim, J. H. Ko, M.-H. Cho, H. Heo, B. Oh, Y. J. Suh, M. J. Kim, D. Na, C. Kim, Y. Kim, S. H. Chun, J. H. Lee, J. Kim, S. Kim, I. Eom, S. N. Kim, T.-Y. Koo, S. Rah,

Y. Shvyd'ko, D. Shu, K.-J. Kim, S. Terentyev, V. Blank, and H.-S. Kang, Hard x-ray self-seeding commissioning at PAL-XFEL, Journal of Synchrotron Radiation **26**, 1101 (2019).

[5] S. Liu, W. Decking, V. Kocharyan, E. Saldin, S. Serkez, R. Shayduk, H. Sinn, and G. Geloni, Preparing for high-repetition rate hard x-ray self-seeding at the european x-ray free electron laser: Challenges and opportunities, Physical Review Accelerators and Beams **22**, 10.1103/physrevaccelbeams.22.060704 (2019).

[6] Z. Huang and R. D. Ruth, Fully coherent x-ray pulses from a regenerative-amplifier free-electron laser, Physical Review Letters **96**, 144801 (2006).

[7] K.-J. Kim, Y. Shvyd'ko, and S. Reiche, A proposal for an x-ray free-electron laser oscillator with an energy-recovery linac, Physical Review Letters **100**, 10.1103/physrevlett.100.244802 (2008).

[8] K.-J. Kim and Y. V. Shvyd'ko, Tunable optical cavity for an x-ray free-electron-laser oscillator, Physical Review Special Topics - Accelerators and Beams **12**, 10.1103/physrevstab.12.030703 (2009).

[9] R. R. Lindberg, K.-J. Kim, Y. Shvyd'ko, and W. M. Fawley, Performance of the x-ray free-electron laser oscillator with crystal cavity, Physical Review Special Topics - Accelerators and Beams **14**, 10.1103/physrevstab.14.010701 (2011).

[10] R. R. Lindberg, K.-J. Kim, Y. Cai, Y. Ding, and Z. Huang, Transverse gradient undulator for a storage ring x-ray fel oscillator, in *Proceeding of FEL2013, New York, NY, USA* (2013) pp. 740–748.

[11] T. Maxwell, J. Arthur, Y. Ding, W. Fawley, J. Frisch, J. Hastings, Z. Huang, and J. Krzywinski, Feasibility study for an x-ray fel oscillator at the lcls-ii, in *Proceedings of IPAC2015* (2015) pp. 1897–1900.

[12] J. Zemella, J. Rossbach, C. Maag, M. Tolkiehn, and H. Sinn, Numerical simulations of an XFELO for the European XFEL driven by a spent beam, in *Proc. of FEL2012, Nara, Japan*, WEPD29 (2012) pp. 429–433, paper WEPD29.

[13] P. Rauer, I. Bahns, W. Decking, W. Hillert, J. Roßbach, and H. Sinn, Integration of an XFELO at the European XFEL facility, Proceedings of the 39th Free Electron Laser Conf. **FEL2019**, Germany (2019).

[14] K. Li and H. Deng, Systematic design and three-dimensional simulation of x-ray FEL oscillator for shanghai coherent light facility, Nuclear Instruments and Methods in Physics Research Section A: Accelerators, Spectrometers, Detectors and Associated Equipment **895**, 40 (2018).

[15] B. W. Adams and K.-J. Kim, X-ray comb generation from nuclear-resonance-stabilized x-ray free-electron laser oscillator for fundamental physics and precision metrology, Physical Review Special Topics - Accelerators and Beams **18**, 10.1103/physrevstab.18.030711 (2015).

[16] W. Qin, K.-J. Kim, R. R. Lindberg, and J. Wu, X-ray FEL Oscillator Seeded Harmonic Amplifier for High Energy Photons, in *Proc. of International Free Electron Laser Conference (FEL'17), Santa Fe, NM, USA, August 20-25, 2017*, International Free Electron Laser Conference No. 38 (JACoW, Geneva, Switzerland, 2018) pp. 196–199.

[17] H. P. Freund, P. J. M. van der Slot, and Y. Shvyd'ko, An x-ray regenerative amplifier free-electron laser using diamond pinhole mirrors, New Journal of Physics **21**, 093028 (2019).

[18] G. Marcus, A. Halavanau, Z. Huang, J. Krzywinski, J. MacArthur, R. Margraf, T. Raubenheimer, and D. Zhu, Refractive guide switching a regenerative amplifier free-electron laser for high peak and average power hard x rays, Physical Review Letters **125**, 254801 (2020).

[19] R. Margraf, Z. Huang, J. MacArthur, and G. Marcus, Microbunch rotation as an outcoupling mechanism for cavity-based x-ray free electron lasers, Proceedings of the 11th International Particle Accelerator Conference **IPAC2020**, 10.18429/JACOW-IPAC2020-WEVIR03 (2020).

[20] P. Rauer, *A Proof-Of-Principle Cavity-Based X-RayFree-Electron-Laser Demonstrator at the European XFEL*, Dissertation, Universität of Hamburg, Hamburg (2022).

[21] Y. V. Shvyd'ko, S. Stoupin, A. Cunsolo, A. H. Said, and X. Huang, High-reflectivity high-resolution x-ray crystal optics with diamonds, Nature Physics **6**, 196 (2010).

[22] For a future upgrade, the crystals shall be exchanged to $t_C \approx 250\,\mu\text{m} to 500\,\mu\text{m}$ thick diamonds, providing more robustness to thermal load.

[23] C. Maag, I. Bahns, J. Rossbach, and P. Thiessen, An experimental setup for probing the thermal properties of diamond regarding its use in an xfelo, in *Proc. of FEL2017, Santa Fe, USA* (2017) pp. 200–203, paper MOP064.

[24] I. Bahns, W. Hillert, P. Rauer, J. Roßbach, and H. Sinn, Interaction of powerful electro-magnetic fields with bragg reflectors, Proceedings of the 39th Free Electron Laser Conf. **FEL2019**, Germany (2019).

[25] B. Yang, S. Wang, and J. Wu, Transient thermal stress wave and vibrational analyses of a thin diamond crystal for x-ray free-electron lasers under high-repetition-rate operation, Journal of Synchrotron Radiation **25**, 166 (2018).

[26] L. Wei, P. K. Kuo, R. L. Thomas, T. R. Anthony, and W. F. Banholzer, Thermal conductivity of isotopically modified single crystal diamond, Physical Review Letters **70**, 3764 (1993).

[27] J. R. Olson, R. O. Pohl, J. W. Vandersande, A. Zoltan, T. R. Anthony, and W. F. Banholzer, Thermal conductivity of diamond between 170 and 1200 k and the isotope effect, Physical Review B **47**, 14850 (1993).

[28] X. Dong, D. Shu, and H. Sinn, Design of a cryo-cooled artificial channel-cut crystal monochromator for the european XFEL, AIP Conference Proceedings **1741**, 040027 (2016).

[29] I. Zagorodnov, M. Dohlus, and S. Tomin, Accelerator beam dynamics at the european x-ray free electron laser, Physical Review Accelerators and Beams **22**, 10.1103/physrevaccelbeams.22.024401 (2019).

[30] W. Decking *et al.*, A MHz-repetition-rate hard x-ray free-electron laser driven by a superconducting linear accelerator, Nature Photonics **14**, 391 (2020).

[31] S. Schulz, M. Czwalinna, M. Felber, M. Fenner, C. Gerth, T. Kozak, T. Lamb, B. Lautenschlager, F. Ludwig, U. Mavrič, J. Müller, S. Pfeiffer, H. Schlarb, C. Schmidt, C. Sydlo, M. Titberidze, and F. Zummack, Few-femtosecond facility-wide synchronization of the European XFEL, Proceedings of the 39th Free Electron Laser Conference **FEL2019**, Germany (2019).

[32] W. Q. Hua, F. G. Bian, Y. M. He, W. H. Lin, L. Song, J. Wang, and N. Zhao, Using the power spectral density method to characterize and evaluate the x-ray mirrors surfaces, in *Proceedings of 4th International Particle*

Accelerator Conference, IPAC 2013, May 13-17, 2013, Shanghai, China (2013).

[33] MXL - Operation of the XFEL Accelerator, Performance - Pulse Energies vs. Photon Energies Overview (2019–2020), `https://xfel.desy.de/operation/performance/`.

[34] J. Alda, Laser and gaussian beam propagation and transformation, in *Encyclopedia of Optical and Photonic Engineering, Second Edition* (CRC Press, 2015) pp. 1–15.

[35] It should be noted, that at pulse energies of $Q_p \approx 70\,\mathrm{mJ}$, the cavity would obviously be strongly affected by heat load.

[36] This estimation is based on the simple product of projected size, projected divergence, projected duration and projected bandwidth. Hence, it can principally strongly deviate from the real phase space volume, as it cannot model strong correlations between position, angle and frequency [63].

[37] J. Krzywiński, Y. Feng, A. Halavanau, Z. Huang, A. Kiss, J. MacArthur, G. Marcus, T. Sato, and D. Zhu, Q-switching of x-ray optical cavities by using boron doped buried layer under a surface of a diamond crystal, Proceedings of the 39th Free Electron Laser Conference **FEL2019**, Germany (2019).

[38] Y. Shvyd'ko, *X-Ray Optics* (Springer Berlin Heidelberg, 2004).

[39] N. Kujala, W. Freund, J. Liu, A. Koch, T. Falk, M. Planas, F. Dietrich, J. Laksman, T. Maltezopoulos, J. Risch, F. Dall'Antonia, and J. Grünert, Hard x-ray single-shot spectrometer at the european x-ray free-electron laser, Review of Scientific Instruments **91**, 103101 (2020).

[40] I. Bahns, Nondestructive interaction of powerfulelectromagnetic waves with bragg reflectors (2021), phD thesis, to be published.

[41] I. Bahns, P. Rauer, J. Rossbach, and H. Sinn, Stability of Bragg reflectors under megahertz heat load at XFELs (2022), to be published.

[42] Z. Qu, Y. Ma, G. Zhou, and J. Wu, Thermal loading on self-seeding monochromators in x-ray free electron lasers, Nuclear Instruments and Methods in Physics Research Section A: Accelerators, Spectrometers, Detectors and Associated Equipment **969**, 163936 (2020).

[43] Generally, the amount of absorbed energy is higher at the downstream crystal than for the upstream one, due to the transmitted spectral side bands being cut off downstream. This leads to a reduced incident pulse energy on the upstream crystal. Also, the transmitted radiation is more strongly absorbed. The heating could nonetheless be approximately matched by reducing the heat conduction efficiency at the upstream crystal, for example by setting a higher base temperature or using a thinner crystal.

[44] D. Meschede, *Optics, Light and Lasers* (Wiley-VCH, 2017).

[45] It has to be noted, however, that in the simulation framework an axial symmetric, very big diamond crystal of ρ=3 cm radius was assumed. As such the heat transfer to the outer boundaries is negligible during one bunch train. For smaller crystals, though, some residual heat would build up also in the X-ray crystal interaction area, which would influence the periodicity of the cavity dumps.

[46] S. Reiche, Genesis 1.3: a fully 3d time-dependent fel simulation code, Nuclear Instruments and Methods in Physics Research Section A: Accelerators, Spectrometers, Detectors and Associated Equipment **429**, 243 (1999).

[47] S. Reiche, *Numerical Studies for a Single Pass High Gain Free-Electron Laser*, phdthesis, Universität Hamburg (1999).

[48] M. Frigo and S. G. Johnson, The design and implementation of FFTW3, Proceedings of the IEEE **93**, 216 (2005).

[49] J. D. Schmidt, *Numerical Simulation of Optical Wave Propagation With Examples in MATLAB*, SPIE Press Monograph, Vol. Vol. PM199 (SPIE Press, 2010).

[50] O. Chubar, M.-E. Couprie, M. Labat, G. Lambert, F. Polack, and O. Tcherbakoff, Time-dependent FEL wavefront propagation calculations: Fourier optics approach, Nuclear Instruments and Methods in Physics Research Section A: Accelerators, Spectrometers, Detectors and Associated Equipment **593**, 30 (2008).

[51] A. Brunetti, M. S. del Rio, B. Golosio, A. Simionovici, and A. Somogyi, A library for x-ray–matter interaction cross sections for x-ray fluorescence applications, Spectrochimica Acta Part B: Atomic Spectroscopy **59**, 1725 (2004).

[52] T. Schoonjans, A. Brunetti, B. Golosio, M. S. del Rio, V. A. Solé, C. Ferrero, and L. Vincze, The xraylib library for x-ray–matter interactions. recent developments, Spectrochimica Acta Part B: Atomic Spectroscopy **66**, 776 (2011).

[53] S. A. Stepanov, E. A. Kondrashkina, R. Köhler, D. V. Novikov, G. Materlik, and S. M. Durbin, Dynamical x-ray diffraction of multilayers and superlattices: Recursion matrix extension to grazing angles, Physical Review B **57**, 4829 (1998).

[54] A. P. Honkanen, C. Ferrero, J. P. Guigay, and V. Mocella, A finite element approach to x-ray optics design, Proc.SPIE **10236**, 11 (2017).

[55] A. G. Shabalin, O. M. Yefanov, V. L. Nosik, V. A. Bushuev, and I. A. Vartanyants, Dynamical effects in bragg coherent x-ray diffraction imaging of finite crystals, Physical Review B **96**, 10.1103/physrevb.96.064111 (2017).

[56] A. Majumdar, Microscale heat conduction in dielectric thin films, Journal of Heat Transfer **115**, 7 (1993).

[57] J. Maassen and M. Lundstrom, Steady-state heat transport: Ballistic-to-diffusive with fourier's law, Journal of Applied Physics **117**, 035104 (2015), http://dx.doi.org/10.1063/1.4905590.

[58] J. Kaiser, T. Feng, J. Maassen, X. Wang, X. Ruan, and M. Lundstrom, Thermal transport at the nanoscale: A fourier's law vs. phonon boltzmann equation study, Journal of Applied Physics **121**, 044302 (2017).

[59] Above orientations are specific to the coordinate system of the mirror assembly and are, depending on the actual rotation of the mirrors, different in the coordinate system of the photon beam.

[60] It should be noted that with this small angle approximation the reflection matrix is not unitary any more. This is fine, as long as the vectors are appropriately normalized after reflection.

[61] G. Giusfredi, *Physical Optics* (Springer, Berlin, 2019).

[62] For the perfect retroreflector all three eigenvalues A, B and C become -1 and, hence, all vectors, being a linear combination of the corresponding set of eigenvectors, return antiparallel to themselves.

[63] J. Bahrdt, Shaping photon beams with undulators and wigglers, in *Synchrotron Light Sources and Free-Electron*

Lasers (Springer International Publishing, 2016) pp. 751–819.